

Article

Feasibility Study of the Bare-Photovoltaic-Tether Concept: Prototypes and Experimental Performance Evaluation of the Photovoltaic Tether Segment

Leo Peiffer¹, Christian Perfler² and Martin Tajmar^{1,*} ¹ Institute of Aerospace Engineering, Technische Universität Dresden, 01307 Dresden, Germany² Sunplugged GmbH, 6413 Wildermieming, Austria

* Correspondence: martin.tajmar@tu-dresden.de; Tel.: +49-351-463-38125

Abstract: Consumable-free electron emitters are presently not feasible for autonomous tether-based deorbit devices such as E.T.PACK due to their power requirement. The bare-photovoltaic-tether (BPT) concept combines the bare tether electron collection with a tether segment, coated with thin film Copper Indium Gallium Selenide solar cells to harvest additional power for the cathodic contact, potentially enabling propellant-less operation. This thesis presents the first prototype of the photovoltaic tether segment, its architecture, its electrical characteristics, major challenges of the system and possible solutions. Photovoltaic tether segments of up to 3 m in length were manufactured, consisting of parallelized submodules of 25 cm in length. Due to space limitations, only the I-V-characteristics of these submodules were measured under a self-built Class BCA LED Solar-Simulator inside a vacuum chamber and at varying temperatures between $-100\text{ }^{\circ}\text{C}$ and $100\text{ }^{\circ}\text{C}$. In addition, the suitability of the concept for a low Earth orbit environment was assessed by performing atomic oxygen exposure tests using a microwave-based low pressure plasma atomic oxygen source. Based on the experimental data, a model is provided for predicting the performance of the photovoltaic segment in orbit, highlighting the main problems of the BPT: temperature, orientation and partial shading.

Keywords: electrodynamic tether; orbital debris; propellant-less CubeSat propulsion; thin film solar cells; CIGS



Citation: Peiffer, L.; Perfler, C.; Tajmar, M. Feasibility Study of the Bare-Photovoltaic-Tether Concept: Prototypes and Experimental Performance Evaluation of the Photovoltaic Tether Segment.

Aerospace **2023**, *10*, 386. <https://doi.org/10.3390/aerospace10040386>

Academic Editor: Vladimir S. Aslanov

Received: 24 February 2023

Revised: 13 April 2023

Accepted: 19 April 2023

Published: 21 April 2023



Copyright: © 2023 by the authors. Licensee MDPI, Basel, Switzerland. This article is an open access article distributed under the terms and conditions of the Creative Commons Attribution (CC BY) license (<https://creativecommons.org/licenses/by/4.0/>).

1. Introduction

Electrodynamic tethers (EDTs) are a promising technology for future space debris avoidance due to potentially propellant-free thrust generation. Therefore, Sánchez-Arriaga et al. proposed the development of a fully passive, fully autonomous and consumable-free tether-based deorbit device [1] capable of deorbiting spacecraft at their end of life. This would combine the propellant-less and passive nature of drag augmentation devices while still providing generally lower deorbit times due to high thrust of EDTs. In terms of autonomy, this is particularly interesting for objects, which do not have their own power source, such as rocket stages or defective satellites.

Using the generator principle, EDTs create an electrical potential difference between the two ends of a long electrical conductor by moving through a planet's magnetic field. In a plasma environment, such as in low Earth orbit (LEO), this potential difference can be used to create a unidirectional current flow in the conductor by closing a circuit between the conductor and the environment. This requires an anodic electron-collecting contact and a cathodic electron-emitting contact. Once a current flow is established, the Lorentz force acts on the current-carrying conductor (called the tether) due to the planetary magnetic field, enabling the generation of thrust or drag depending on the direction of the current.

The state-of-the-art approach for anodic contact is the bare tether principle, which passively collects electrons [2]. The cathodic contact, on the other hand, is still based on active electron emitters, of which three major technologies are feasible and require an

external power supply: hollow cathode plasma contactors, thermionic electron emitters and field emission electron emitters. The former are usually feasible for high currents, and require low amounts of power and additional expellant [3]. The latter two technologies are available as completely consumable-less devices for low currents, which require high amounts of power due to space charge effects. This power requirement would reduce the compactness of autonomous EDT-based deorbit devices, requiring additional assembly and storage space for dedicated solar panels and thus reducing competitiveness in comparison with other propellant-less deorbit devices such as electrostatic plasma brakes [4].

A cathodic contact for propellant-less EDTs has also been discussed in the frame of low work function tethers, which are envisaged to passively emit electrons under solar irradiation via thermionic [5] and photoelectric [6] effects but are not yet feasible.

In 2021, Tajmar and Sánchez-Arriaga proposed the bare-photovoltaic-tether (BPT) concept), which aims to take advantage of the progress in thin film solar cell technologies to use the surface area of the electrodynamic tether for solar energy harvesting, thus enabling the use of active electron emitters without a propellant [7]. Modern EDTs use tapes instead of wires, due to better performance and higher impact survival probabilities [8], thus providing a suitable flexible substrate for thin film solar cells. Due to the thin film nature of the solar cells, the increase in available power would only come at the cost of additional mass, but without decreasing the compactness of the EDT system.

The original BPT proposed to couple the electrical circuit of both the EDT and the photovoltaic cells in order to increase the performance of the EDT by increasing the electrical potential difference between its two ends. However, this coupling carries a high risk of total system failure, as a malfunctioning of the photovoltaic circuit also impairs the current flow in the EDT; therefore, decoupling the two circuits was proposed [9]. By decoupling both circuits, the BPT would then include an additional photovoltaic tether segment (PTS), which would act as a tether-shaped solar panel, harvesting additional power to increase the autonomy of an EDT-system, while the current of the EDT would flow through the electrically conductive substrate of the solar cells. In the event of failure of the photovoltaic circuit, the current flow in the tether would remain guaranteed. No additional support structure would be required; therefore, the theoretically achievable specific power (power per mass) would be high compared to conventional solar panels. Assuming an EDT with a total length of 1 km, a PTS length of 500 m and a width of 2 cm, a surface area of 10 m² could be used for power harvesting. Record module efficiencies of mature thin-film technologies such as Copper-Indium-Gallium-Selenide (CIGS) reach values of up to 19.2% at 25 °C [10]. Hence, in an unrealistic best-case scenario, a promising 2.6 kW of power could be achieved with a PTS. In the usual scenario, however, the PTS will never be optimally oriented towards the sun due to twisting, and the module efficiency will be highly reduced not only due to much higher temperatures in space but also due to the unconventional tether-shape, which limits the available installation space for proper busbar systems and thus detrimentally influences the current-voltage characteristic of the PTS due to unfavorable ohmic resistances.

This study presents a design of the PTS that combines the CIGS thin-film solar cell technology with a bare aluminum tether that is compatible with partial shading resulting from suboptimal tether orientation and torsional twisting. Its fabrication based on monolithic module integration is outlined. In addition, the three major negative effects on the PTS performance, high temperatures, atomic oxygen and torsional twisting, are experimentally evaluated to realistically discuss the in-orbit performance and the feasibility of a PTS.

2. Materials and Methods

2.1. The PTS Design and PTS Samples

The PTS is integrated into the EDT, using a polyimide layer as a substrate for the thin film solar cells and as an insulating barrier to the bare aluminum tether. Typically, flexible CIGS solar cells are grown either on stainless-steel sheets with a thin film insulating

glass layer or directly on polyimide sheets. Stainless-steel as an electrically conductive substrate has been discussed as a promising solution for PTS, as the EDT current could be carried by the stainless-steel layer while the glass insulator decoupled the photovoltaic circuit [9]. In addition, CIGS solar cells on stainless-steel generally achieve higher power conversion efficiencies, due to higher process temperatures, thus leading to beneficial crystal growth [11]. However, stainless-steel has more than twice the density of bare aluminum, a significantly lower electrical conductivity, and its use in a PTS creates the problem of joining the PTS substrate to the bare aluminum tether of the EDT. As shown in Figure 1, the PTS of this study includes a polyimide layer as both a direct substrate for the thin-film solar cells and an insulator to decouple the two electrical circuits. The cells consist of a transparent conductive oxide (TCO) front contact, in this case Aluminum-doped Zinc-Oxide (AZO), the CIGS graded absorber crystal, and a molybdenum back contact. The front contact is supported by a silver grid to enhance electron collection and to reduce ohmic losses.

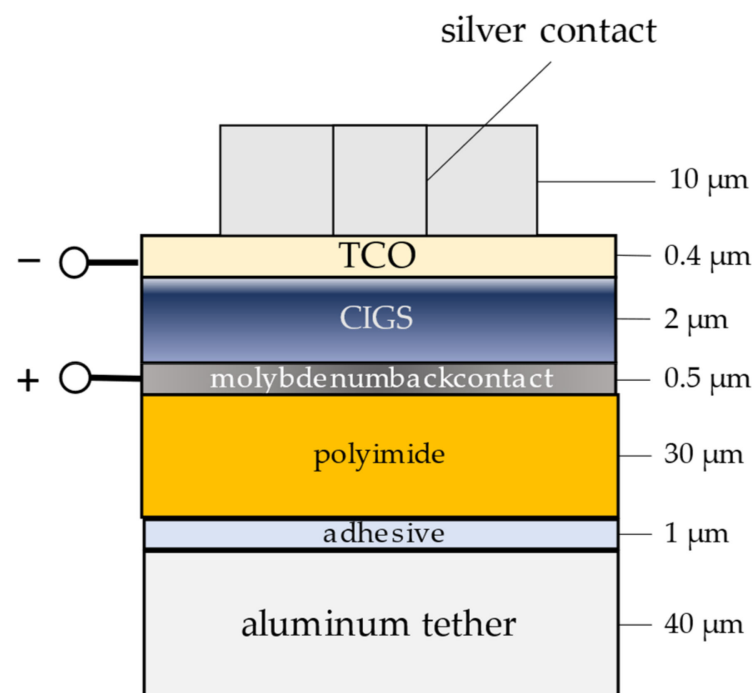


Figure 1. PTS layering: The solar cells consist of a transparent conductive oxide (TCO) layer as a front contact, the Copper–Indium–Gallium–Selenide (CIGS) absorber material and a molybdenum back contact. The front contact is supported by a silver electron collecting grid. The cells are grown on a polyimide substrate, which is applied to a bare aluminum tether, using an adhesive transfer tape; dimensions are not to scale.

Before the silver electron collecting grid is applied and the cell stack is mounted on the aluminum tether, the cell layers are patterned into submodules via monolithic integration [12]. These patterns can be freely adapted to meet the actual use-case requirements. In this study, these submodules were designed in to have a maximum power point voltage of 28 V at 25 °C and to be connected in parallel. After monolithic integration, the submodules are applied to the aluminum tether using adhesive transfer tape. They are interconnected by two lateral busbars, which are applied after sealing to the gaps between each submodule with an insulating material (see Figure 2). They also serve as electrical contacts to the spacecraft.

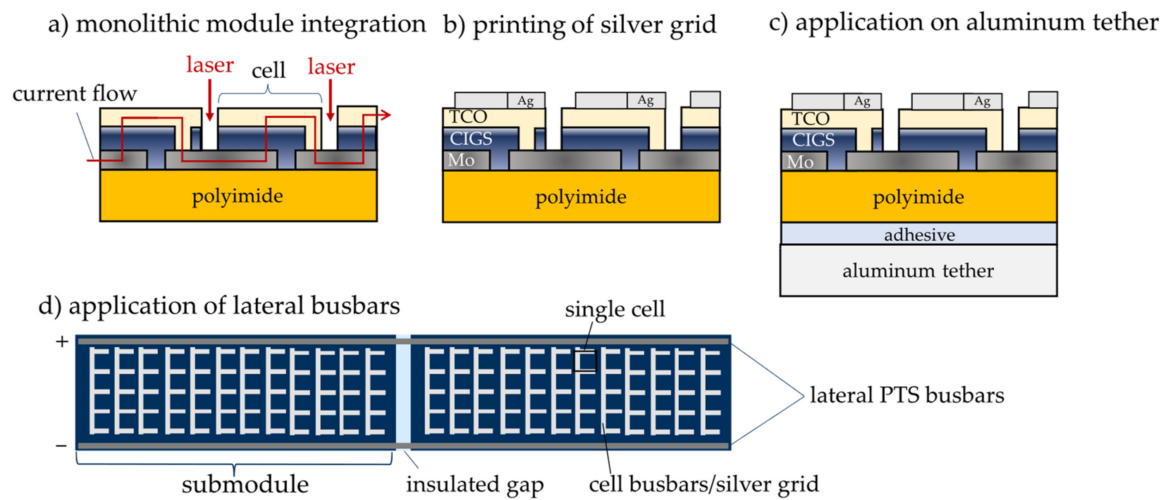


Figure 2. PTS fabrication: (a) laser-based monolithic integration of submodules; (b) application of silver grid in an ink jet printing process; (c) application of the cells with substrate to the bare aluminum tether using; (d) application of lateral busbars for parallelization of submodules and contacting to the spacecraft.

The parallel connection of the submodules to the lateral busbars is not visible from the outside and was also realized with laser structuring. The reason for this PTS architecture is a partial shading issue, resulting from torsional twisting of the PTS along the tether line after deployment. However, this torsional twisting is both detrimental and beneficial to the performance of the PTS. On the one hand, it reduces the active photovoltaic area; on the other hand, it reduces the negative effects of a sub-optimal tether orientation (e.g., when the pv area is facing away from the sun). As a result, the twisted PTS power is lower but more stable. Applying the solar cells on both sides of the tether is not feasible for two reasons. First, the solar cells have a preferred bending direction and would therefore crack if applied on both sides. Second, the electron collection capability of the bare aluminum tether would be reduced, if not completely lost, in the region of the PTS.

However, partial shading prohibits the serial connection of submodules along the tether line because the current voltage characteristic of a serial connection of solar cells or entire modules is dominated by its weakest link, and thus by the least illuminated element of the connection. If a PTS of serially connected submodules had torsional twists along the tether line, its performance would drop to zero even if only one of the submodules was in shadow. This could be avoided by adding bypass diodes to each submodule. However, they would increase the thickness of the PTS, reducing its flexibility, and making it a vulnerable but indispensable element. Instead, the PTS of this study includes submodules connected in parallel. When submodules are shaded or inside the transition zone between light and shadow, their performance drops to zero, while illuminated submodules still contribute to the total power output of the PTS. The PTS power of the parallel configuration would only decrease in proportion to the shaded photovoltaic area, instead of dropping to zero as in a serial configuration. This is an oversimplification of the process because the irradiance on the photovoltaic area changes with the angle of incidence; therefore, there are further detrimental effects of twisting. These effects are discussed in the experimental section below.

In this study, the electrical characteristics of six 25 cm long and 2.5 cm wide submodules were evaluated under the influence of vacuum and temperature. In addition, a 1.5 m long PTS sample, consisting of six submodules of the same type, which were connected in parallel, was tested against the influence of twisting. Figure 3 shows one of the coiled-up submodules on the right side and the 1.5 m PTS sample on the left side.

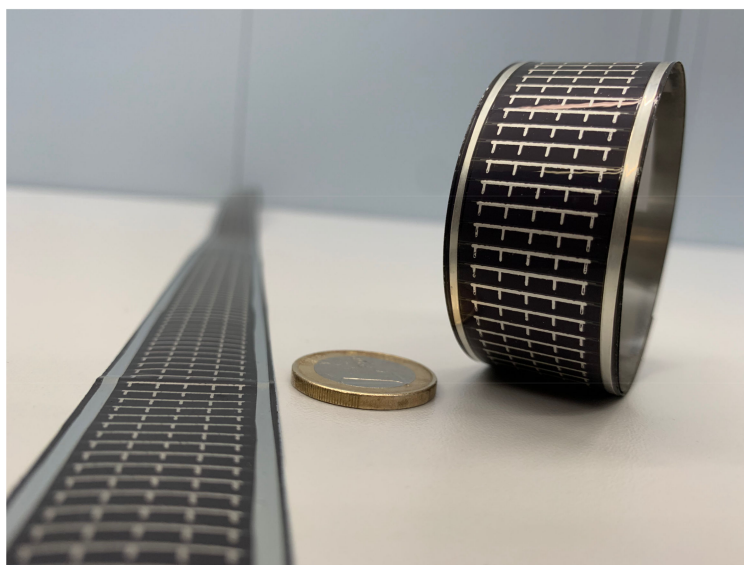


Figure 3. PTS sample with a length of 1.5 m on the left; submodule with a length of 25 cm on the right; the total thickness of the samples is 103 μm (including lateral busbars); a submodule consists of 80 serially connected strings of four parallelized cells each.

These samples have a total thickness of 103 μm , including the lateral busbars. The busbars are made of a conductive copper tape 20 μm thick and 2 mm wide. Their mass per unit length is 6 g/m compared to 2.7 g/m for the bare 40 μm aluminum tether. The key parameters of the six submodules are shown in Table 1. First, the efficiency η_0 is shown, measured with a Keithley 2420 Source Measurement Unit (SMU) under a g2voptics Sunbrick Solar Simulator (SoSi) at 25 $^{\circ}\text{C}$ and Air-Mass 0 (AM0) spectrum (1367 W/m^2). Second, the electrical parameters, open circuit voltage V_{oc} and short circuit current I_{sc} , as well as the maximum power point voltage V_{MPP} and current I_{MPP} , are presented. Third, the fill factor (FF) is presented, which is the ratio between the product of the maximum power point parameters $I_{\text{MPP}} \times V_{\text{MPP}}$ and the product of the open circuit voltage and short circuit current $V_{\text{oc}} \times I_{\text{sc}}$ and is a measure of the quality of the photovoltaic cells. In addition, the serial resistance R_s and parallel resistance R_p of each submodule are indicated, since they directly influence the FF.

Table 1. Key parameters of the six submodules, investigated in this study: efficiency η_0 , measured at 25 $^{\circ}\text{C}$ and AM0 (1367 W/m^2), open circuit voltage V_{oc} , short circuit current I_{sc} , maximum power point voltage V_{MPP} , maximum current I_{MPP} . Fill factor (FF), serial resistance R_s , parallel resistance R_p .

Sample	η_0 [%]	V_{oc} [V]	V_{MPP} [V]	I_{sc} [mA]	I_{MPP} [mA]	FF [%]	R_s [Ω]	R_p [k Ω]
AI-1	5.64	39.09	27.24	16.82	14.19	58.79	537	96.25
AI-2	5.15	40.44	26.25	16.67	13.45	52.37	655	137.68
AI-3	6.06	41.16	28.41	17.19	14.61	58.70	568	167.42
AI-4	4.70	36.22	25.59	15.78	12.59	56.34	463	89.53
AI-5	5.71	39.70	27.45	16.89	14.25	58.35	568	60.80
AI-6	6.01	39.38	27.91	17.33	14.76	60.36	455	176.13
mean	5.55	39.33	27.14	16.78	13.98	57.49	541	121.30

The efficiencies of the submodules cannot compete with state-of-the-art CIGS module efficiencies between 12% and 15% [10]. This is mainly due to a high serial resistance and a low parallel resistance, which increase dissipation and shunt losses, respectively. The detrimental serial resistance can be attributed to the high number of serially connected cells, whereas the low parallel resistance may be a result of the lateral PTS busbars, which cover the entire length of the submodules and thus provide a high contact area for shunting.

The average efficiency of the PTS submodules of CIGS cells on polyimide applied to a bare aluminum tether was lower than that reported for PTS submodules of CIGS cells on stainless-steel (7%), which serves as both the cell substrate and the electrical conductor for the EDT over the length of the PTS [9].

When connecting these submodules in parallel in a PTS, it is important that they have the same or at least similar current–voltage (I–V) characteristics, so that the operating point of the overall PTS is compatible with each individual submodule. Matching the submodules at this stage of development is time-consuming and costly due to the creation of rejects by the non-optimized manufacturing process. For example, in a batch of twelve submodules, seven samples had a deviation in I_{MPP} or V_{MPP} of more than 5% and up to 45% from the envisaged values. Therefore, there was no well-matched and optimized PTS available yet. The 1.5 m PTS in this study consisted of poorly matched submodules and was primarily fabricated for mechanical testing, which is not the focus of this work. In addition, a dedicated solar simulator setup covering the full 1.5 m length with adequate illumination was not available. As a result, there are no reliable data available on the maximum performance of the 1.5 m PTS. However, the qualitative influence of torsional twisting on PTS performance was evaluated in a dedicated twisting setup.

2.2. Material Demonstrators

The silver electron collecting grid of the PTS is not suitable for a low Earth orbit (LEO) environment due to its susceptibility to atomic oxygen. The polyimide substrate, which is also susceptible to atomic oxygen, is protected from both sides (aluminum tether/photovoltaic cells), while the silver grid is directly exposed to atmospheric influences. Therefore, seven material demonstrators were provided and investigated to find a way to increase the robustness of the front contact against atomic oxygen. The different front contacts of the demonstrators are shown in Figure 4.

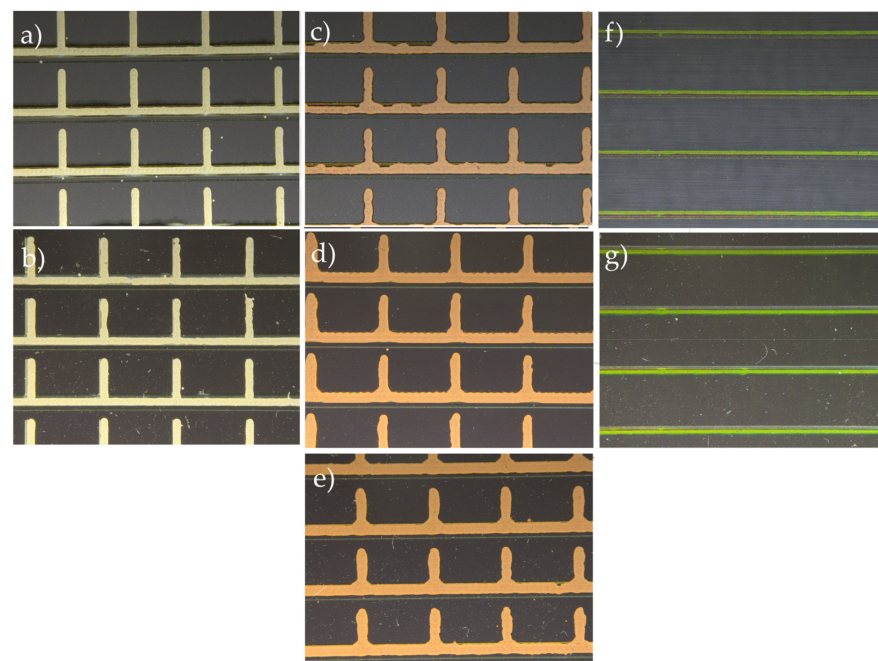


Figure 4. Material demonstrators: (a) Ag grid, AZO as front contact; (b) Ag/AZO, coated with silicate-based Sol-gel; (c) Cu grid, AZO as front contact; (d) Cu/AZO, coated with a silicate-based Sol-gel; (e) Cu/AZO, coated with CAG37; (f) no grid, ITO as front contact; (g) ITO, coated with a silicate-based Sol-gel.

Three approaches are considered to overcome the atomic oxygen susceptibility: using copper ink instead of silver ink for the electron collecting grid, using protective coatings, or

not using an electron collecting grid at all. Therefore, the material demonstrators differed in the grid material (Silver or Copper), the coating (none, Sol-gel, CAG37 by durXtreme) and the TCO. For the latter, Aluminum-doped Zinc Oxide (AZO) and Indium Tin Oxide (ITO) were used. Table 2 summarizes the different material combinations and shows the average efficiency of the samples at standard test conditions (STC). The samples had a square shape with a side length of 35 mm and did not contain a polyimide layer. The solar cells of all material demonstrators were deposited on stainless-steel.

Table 2. Material combinations of the material demonstrators for atomic oxygen tests; Ag–Silver, Cu–Copper, Aluminum-doped Zinc Oxide (AZO), Indium Tin Oxide (ITO).

No.	Grid	TCO	Coating	η_m [%]
1	Ag	AZO	-	6.05
2	Ag	AZO	Sol-Gel	6.62
3	Cu	AZO	-	7.93
4	Cu	AZO	Sol-Gel	6.37
5	Cu	AZO	CAG37	6.37
6	-	ITO	-	4.74
7	-	ITO	Sol-Gel	5.28

The highest average efficiency (7.93%) was achieved with material combination 3 (Cu/AZO, no coating). Material combinations 5 and 6 showed the lowest efficiencies (4.74%, 5.28%), indicating the positive influence of the electron collecting grid. The influence of the coatings on the mean efficiency was not clear, as they had either a positive (no. 2 and 7) or negative effect (no. 4 and 5).

2.3. Solar Simulator (SoSi) Setup

The self-built SoSi (Figure 5) was designed to illuminate an area of 32 cm × 8 cm on a thermal plate at a distance of 10 cm inside a vacuum chamber, allowing temperature control of the illuminated samples and vacuum exposure. The light source was based on light emitting diodes (LEDs) and consisted of four LED clusters, each consisting of 22 LEDs with 16 different peak wavelengths ranging from 270 nm to 1100 nm (see Appendix A). Each cluster was surrounded by four square-shaped SEA-UV broadband surface mirrors from Präzisions Glas & Optik with the intention of homogenizing and guiding the light. The design of the light source was based on the works of Mohan et al. [13] and Linden et al. [14]; however, it was less elaborate due to lower measurement uncertainty requirements. The LEDs were soldered to aluminum printed circuit boards (PCB) mounted on liquid-cooled aluminum heat sinks. The aluminum thermal plate was flushed with either water or liquid nitrogen (LN₂). In addition, two 10 W heating foils were applied to the back of the thermal plate to control its equilibrium temperature, which was influenced by the liquid cooling, the irradiance of the SoSi, and the heaters.



Figure 5. Left: SoSi in front of vacuum chamber; right: Four LED clusters and light guides; liquid cooling system for the LEDs.

According to the IEC standards for simulator performance requirements [15], this solar simulator was rated Spectral Match (SM) Class B in the wavelength range 400 nm to 1000 nm for the AM0 spectrum, Spatial Uniformity (SNU) Class C in an area of 4 cm × 32 cm and a Temporal Stability (TS) of Class A. The spectral irradiance of the SoSi was determined using a Qmini RGB Photonics (Wide UV) spectrometer in combination with the current signal from a calibrated FDS100-CAL photodiode from Thorlabs. The spectral irradiance $E(\lambda)$ [W/m²nm] of the SoSi was calculated using Equation (1) with the measured normalized spectrum $S_n(\lambda)$ [1/nm] of the SoSi, the spectral sensitivity $R_{ph}(\lambda)$ [A/W], the current output I_{ph} [A], and the active area A_{ph} [m²] of the photodiode.

$$E(\lambda) = \frac{I_{ph}}{A_{ph} \int S_n(\lambda) R_{ph}(\lambda) d\lambda} S_n(\lambda) \tag{1}$$

The spectral irradiance of the SoSi is shown in Figure 6 in comparison to the AM0 spectrum of the Sun. The measurement was made in the center of the 8 cm × 8 cm test area at a distance of 10 cm below one of the LED clusters.

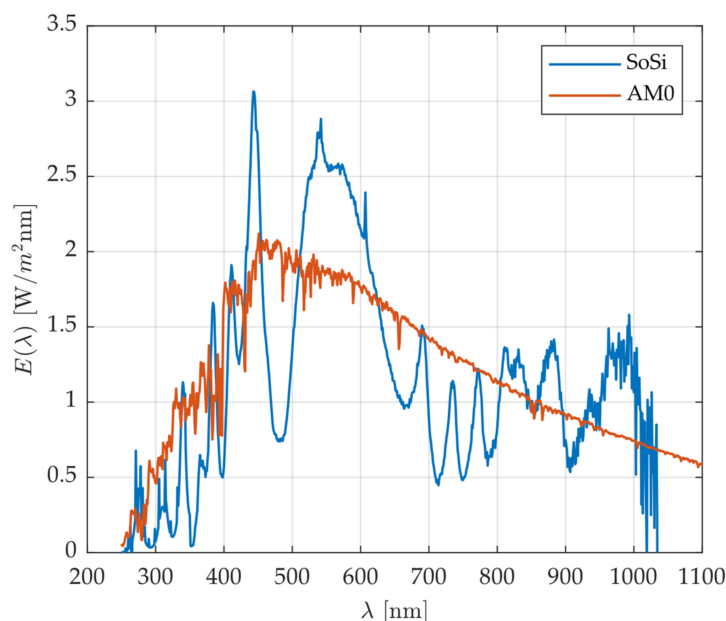


Figure 6. Spectral irradiance $E(\lambda)$ of the SoSi in comparison to Sun’s AM0 spectral irradiance.

The spectrometer used for this measurement covers a wavelength range from 250 nm to 1000 nm. Therefore, insufficient data were collected above 1000 nm. In Table 3, the irradiance of the SoSi in the wavelength range 200 nm to 1100 nm is compared to the irradiance of the Sun with an interval width of 100 nm.

Table 3. Comparison of the irradiance of the SoSi and Sun’s AM0 spectrum in the range 200 nm to 1100 nm; Spectral Match $SM = E_{SoSi}/E_{AM0}$; classification according to the IEC [15].

Interval [nm]	E_{SoSi} [W/m ²]	E_{AM0} [W/m ²]	SM	Class
200–300	6.7	14.4	0.47	C
300–400	52.6	95.7	0.55	C
400–500	152.5	188.4	0.81	A
500–600	231.2	186.5	1.24	A
600–700	140.8	160.4	0.88	A
700–800	77.3	128.8	0.60	B
800–900	116.3	102.4	1.14	A
900–1000	103.5	83.4	1.24	A
1000–1100	27.5	66.7	0.41	C
Total:	908.2	1026.5	-	-

In the range from 200 nm to 1100 nm, the SoSi therefore only achieves SM class C, while in the 400 nm to 1000 nm range, it achieves class B with a maximum deviation of 40% in the 700–800 nm interval. The total irradiance of the SoSi in the full wavelength range is 10% lower than the irradiance of the sun in the same range.

The spatial non-uniformity (SNU) is a measure of how uniformly the irradiance of the SoSi is distributed in the test plane. It is calculated using Equation (2) according to IEC [15].

$$\text{SNU} = \frac{E_{\max} - E_{\min}}{E_{\max} + E_{\min}} \times 100\% \quad (2)$$

In Equation (2), E_{\max} and E_{\min} are the maximum and minimum irradiances measured in the test plane, respectively. The SNU of the SoSi was determined by measuring the photocurrent of the calibrated FDS100-CAL photodiode at 64 equidistant points in the $8 \text{ cm} \times 8 \text{ cm}$ test plane below each LED cluster. This results in an 8×8 matrix that can be plotted as a contour plot. Figure 7 shows a contour plot of the spatial distribution of the irradiance in the $8 \text{ cm} \times 8 \text{ cm}$ test plane under a LED Cluster. At each position, the measured local irradiance E' is compared to the mean irradiance E_m in the plane as the ratio E'/E_m . The contour lines indicate zones of similar irradiance. Each boundary indicates its numerical threshold value. For example, the zone inside the 1.1 boundary means that the local irradiance is higher than the mean irradiance by a factor between 1.1 and 1.15. However, this plot does not directly visualize the spatial uniformity of the irradiance, but only provides a descriptive impression. According to Equation (2), the SNU of the $8 \text{ cm} \times 8 \text{ cm}$ plane is 15.1% and thus a failure of the SNU criterion. However, in the zone of Figure 7 between $x = 3$ and $x = 7$ and in the entire y -range, the SNU is 9.7% which is sufficient for class C. The spatial distribution of irradiance was nearly the same for all four LED clusters, so that the distribution of irradiance for the full $8 \text{ cm} \times 32 \text{ cm}$ test plane can be obtained by stringing together the plot of Figure 7 four times in the y -direction.

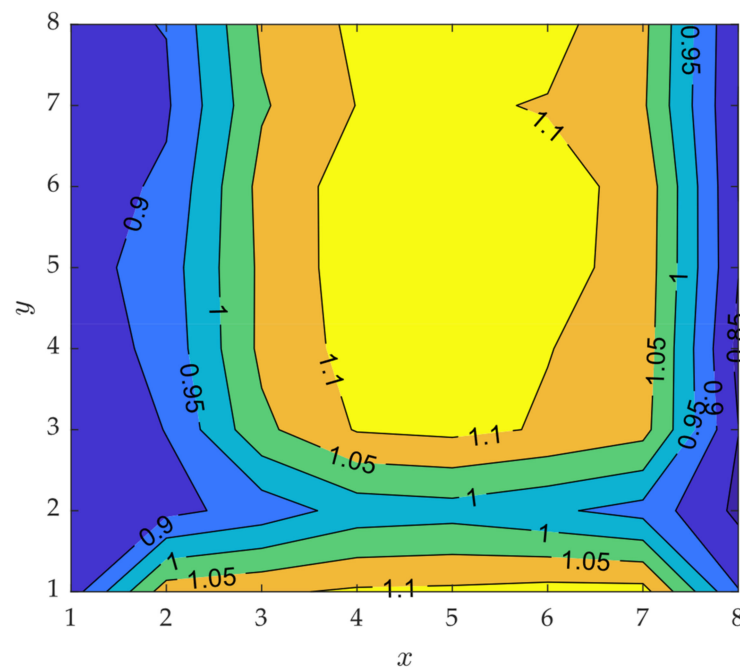


Figure 7. Spatial distribution of irradiance: the local irradiance E' is compared to the mean irradiance E_m of the $8 \text{ cm} \times 8 \text{ cm}$ test plane under a representative LED cluster at 64 equidistant points; the diagram shows a contour plot, indicating zones where the ratio $R = E'/E_m$ lies between the given limits; the axes of the plot indicate the dimensionless location of the measurement points; the $8 \text{ cm} \times 8 \text{ cm}$ area was divided into 64 equidistant squares; the intensity measurements were made at the center of each square.

The temporal stability (TS) was determined by continuously measuring the photocurrent of the FDS100-CAL photodiode with a Keithley 2450 SMU. The photodiode was placed in the center of one of the 8 cm × 8 cm test planes. After 30 min of measurement, the TS was determined to be 0.06%, fulfilling the class A criterion.

Due to the non-optimized spectral match, the spatial non-uniformity of the irradiance and the non-collimated light source of the self-built solar simulator, it is not suitable for precise calibrations and measurements in the specific field of solar cell development. However, it was suitable for a qualitative analysis of the electrical characteristics of the PTS at different temperatures in a limited area of 4 cm × 32 cm.

2.4. Atomic Oxygen Exposure Facility

The atomic oxygen exposure facility (ATOX), shown in Figure 8, was originally built for the development and calibration of atomic oxygen sensors [16]. It is based on a low-pressure plasma atomic oxygen source and has a 15 × 15 × 15 cm³ vacuum chamber for the samples under investigation. Atomic oxygen, among other gaseous species, is generated in a dedicated plasma chamber and released into the vacuum chamber through an orifice. In the reference plane, located 45 mm from the plasma chamber outlet, an atomic oxygen flux of $(2.85 \pm 0.46) \times 10^{14}$ Atoms/cm²s over a 10 mm × 10 mm area was determined using Kapton[®] HN 200 samples. The detailed calibration procedure can be found in the Supplementary Materials of this article. Since the atomic oxygen source is based on a low-pressure plasma (1 mbar) and the flow between the plasma chamber and the vacuum chamber is in the transition flow regime, the kinetic energy of the atomic oxygen is estimated to be less than 0.5 eV.

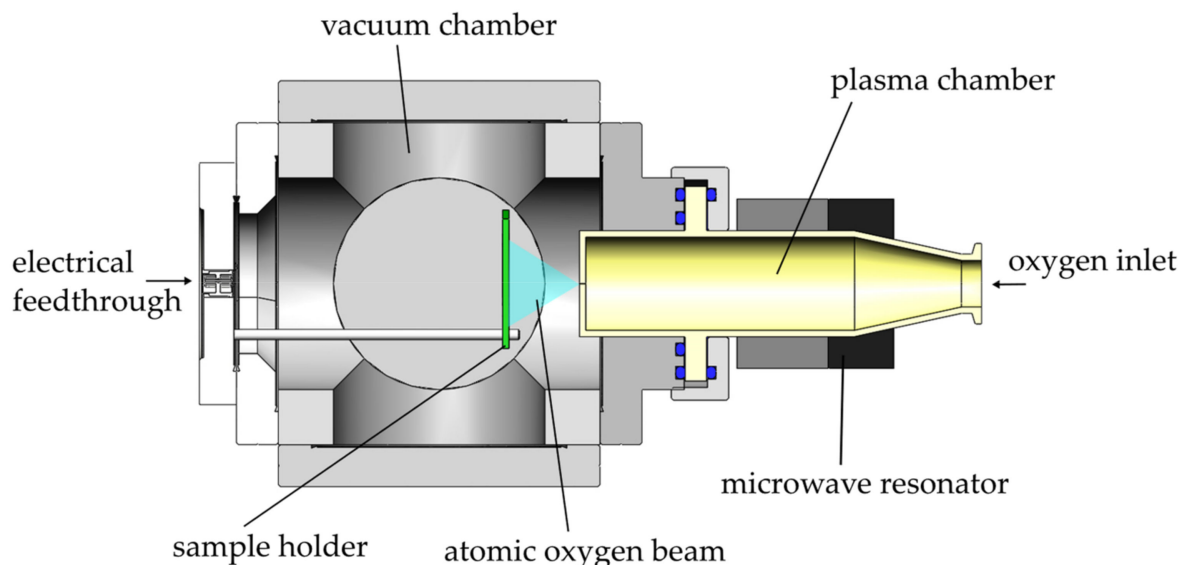


Figure 8. Overview of the atomic oxygen exposure facility (ATOX); atomic oxygen is generated in a microwave-based low-pressure oxygen plasma and released into a vacuum chamber, creating a flow of atomic oxygen and other gaseous species to a sample.

2.5. Twisting Setup

The PTS is expected to twist arbitrarily along the tether line in space due to the EDT-deployment. Since the tether can be thought of as a torsion spring, this twisting will vary with time (number of twists per length). The irradiance on a surface depends on the angle of light incidence. If the surface of the PTS is assumed to be uniformly twisted along its length, the irradiance on that surface is reduced by a factor of $1/\pi$ (0.32) compared to the case, in which the entire PTS surface is orthogonal to the incident light over the entire length. In addition, the reflection behavior also depends on the angle of light incidence.

The submodules of the PTS will therefore experience suboptimal and constantly changing illumination conditions, which will affect the overall I-V characteristic of the PTS.

A setup was constructed to qualitatively evaluate the influence of torsional twists on the performance of the PTS. The setup is shown in Figure 9. It features two mechanical fixings for the 1.5 m PTS. One of the fixings can be freely rotated to simulate the twisting. The other has an electrical connection to a Keithley 2450 SMU.

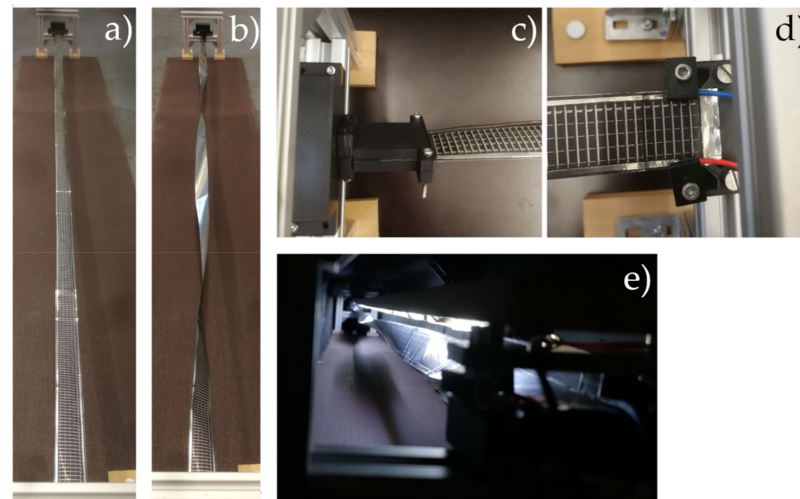


Figure 9. Twisting setup: (a) 1.5 m PTS without twisting; (b) 1.5 m PTS with 0.67 twists/m; (c) rotatable mechanical fixing; (d) mechanical fixing with electrical connection; (e) full setup with twisted PTS placed under an LED strip inside a black box to avoid external light incidence.

The PTS was clamped between these two fixings and placed under a light source inside a cardboard box that was completely painted black to reduce light reflections and external light incidence. The light source consisted of a cool white LED strip with a radiant power of 550 Lumen/m which equals around 4.4 W/m. As a rough estimate, the irradiance on the PTS at a distance of 3 cm from the light source was determined to be 42 W/m², considering an LED aperture half angle of 60°. The light source was not collimated.

The normalized irradiance $E'(L)$ along the twisted PTS with a length L_0 of 1.5 m can be described as in Equation (3) for this experimental setup.

$$E'(L) = \frac{E(L)}{E_0} = \cos\left(2\pi n \frac{L}{L_0}\right) \quad (3)$$

E_0 is the undisturbed irradiance of the light source on an orthogonal surface and n is the number of twists over the entire length. The cosine relation results from the fact that the PTS is fixed on one side so that the PTS surface is always orthogonal to the light source at this point of fixation. Equation (3) can be used to plot the irradiance on the photovoltaic surface of the PTS against the longitudinal coordinate L , a function of the number of twists n . Integrating E/E_0 over the entire length of the PTS for different n and considering only the positive share of the graph gives the percentage of radiant power received by the twisted PTS compared to a PTS without any twists ($n = 0$). This would lead, e.g., to a percentage of 63.71% for $n = 0.25$, 31.93% for $n = 1$ or 38.25% for $n = 1.25$. This model was used to evaluate the experimental results presented below and to assess whether the power output of an evenly twisted PTS can be simply described with a loss factor of $1/\pi$ or whether additional considerations need to be made.

3. Results

3.1. Influence of Temperature on the PTS Submodules

The PTS submodules of Table 1 were placed on the thermal plate of the SoSi setup. Thermal contact between a sample and the thermal plate was established using Arctic

Silver Céramique 2 thermal paste. The temperature of the samples was measured using a type K thermocouple in combination with an MC USB Temp data acquisition device. The thermocouple was applied to the aluminum substrate of the submodules using a 3M Scotchweld 2216 two-component epoxy resin adhesive for direct thermal coupling (see Figure 10).

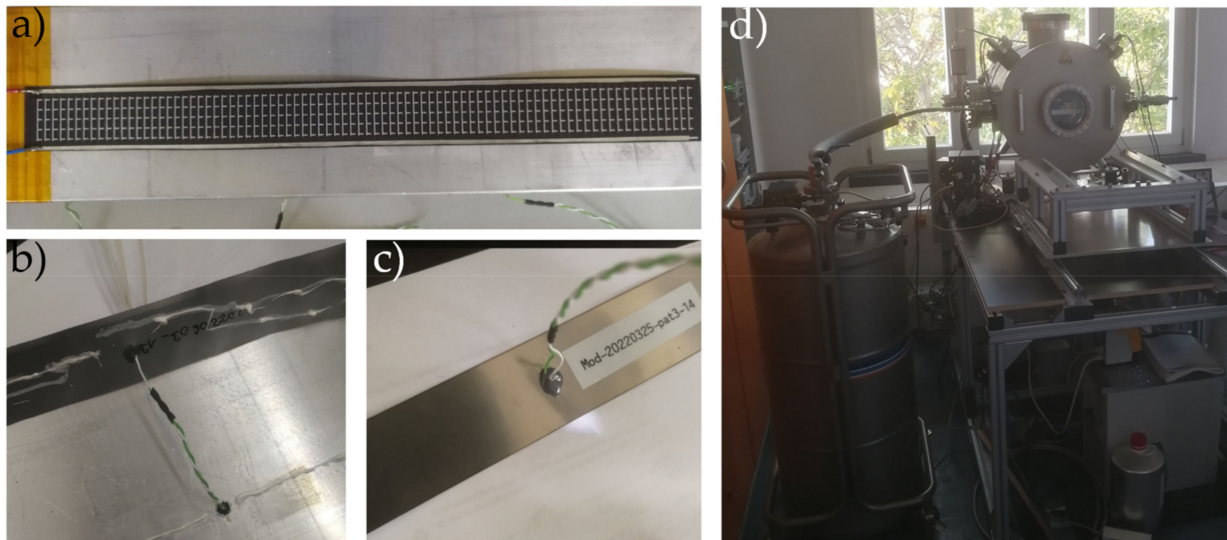


Figure 10. Sample preparation: (a) PTS submodule mounted on the thermal plate of the SoSi setup; (b) application of thermal paste; (c) curing joint between thermocouple and sample; (d) LN₂ Dewar container connected to vacuum chamber.

After the thermal plate was installed under the SoSi inside the vacuum chamber and the vacuum was generated, the thermal plate was flushed with liquid nitrogen (LN₂) until the sample temperature had cooled to $-105\text{ }^{\circ}\text{C}$. With the SoSi switched on, the sample temperature increased to the point where it could be manually controlled with the flow of LN₂ through a valve. The temperature measurement uncertainty was $\pm 1.5\text{ K}$, while the temperature offset of the true solar cell temperature was estimated to be $+5\text{ K}$, due to the thin film nature of the PTS layering and the mediocre thermal conductivity of the epoxy resin adhesive.

This offset was investigated by measuring the steady-state temperature difference between two thermocouples attached to the photovoltaic area and the aluminum tether. These measurements were performed under irradiation of the SoSi and in vacuum. While the thermocouple on the aluminum side was attached using the epoxy adhesive as described above, the thermocouple on the top side was attached to the photovoltaic area using 235—3M Black adhesive tape. For both the hot and cold cases, a temperature difference of $+2\text{ K}$ was measured between the PV side and the aluminum side. However, since the CIGS layer ($\alpha/\varepsilon = 3$ [17]) has a higher α/ε ratio than the 235—3M Black Adhesive Tape ($\alpha/\varepsilon = 1.05$ [18]), it was concluded that the true temperature of the cells, and thus the temperature difference between the measurement point on the aluminum tether and the pv area, must be even higher. Following this conclusion, the measurement offset was multiplied by a factor of 2.5 ($\Delta T_{\text{Offset}} = +5\text{ K}$) and not further evaluated. In the main experiment, the sample temperature was raised from $-100\text{ }^{\circ}\text{C}$ to $100\text{ }^{\circ}\text{C}$, supported by the additional heating foils. Every 20 K, the I-V characteristic of the tested submodule was measured using the sweep function of the Keithley 2450 SMU. Six different submodules were tested. The exemplary I-V characteristics of the Al6 sample at temperatures between $-100\text{ }^{\circ}\text{C}$ and $100\text{ }^{\circ}\text{C}$ are shown in Figure 11.

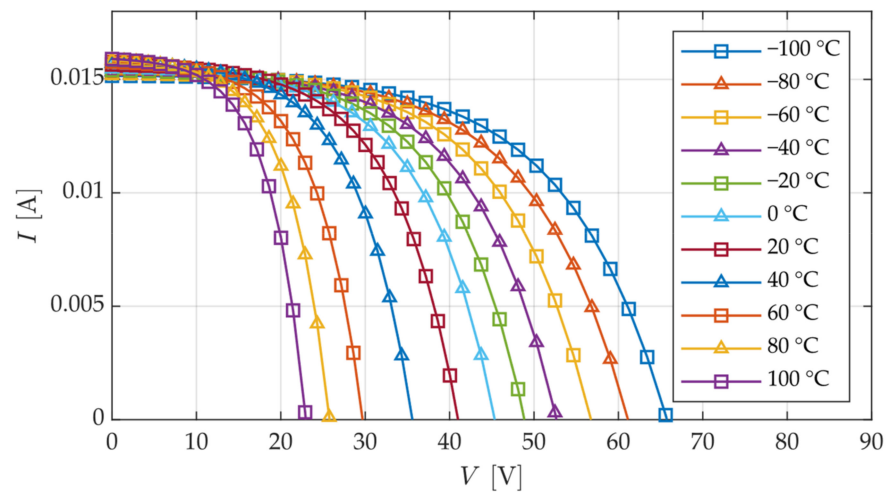


Figure 11. I-V characteristic of sample Al 6 at different temperatures in the fourth quadrant; measurement with Keithley 2450 SMU's sweep function under Class BCA Solar Simulator with irradiance 908.2 W/m^2 in wavelength range 200 nm to 1100 nm.

As expected, the results indicate that the performance of the PTS submodules decreases with increasing temperature. Table 4 shows the normalized temperature coefficients for several parameters of the submodules. The normalization followed the method of Theleen et al. [19], where the temperature coefficient of the quantities, as the efficiency, was related to the quantity at $25 \text{ }^\circ\text{C}$. In the case of the present study, the reference values at $20 \text{ }^\circ\text{C}$ were used.

Table 4. Arithmetic means of the normalized temperature coefficients dX/dT for different quantities: power conversion efficiency η , fill factor FF, open circuit voltage V_{oc} and short circuit current I_{sc} ; six PTS submodules were investigated; normalization refers to the quantities at $20 \text{ }^\circ\text{C}$; standard deviation σ .

Quantity X	dX/dT [%/K]	σ [%/K]
Efficiency η	−0.448	0.021
Fill Factor FF	−0.026	0.027
Open Circuit V_{oc}	−0.456	0.024
Short Circuit I_{sc}	+0.027	0.004

Except for the FF, these results were in agreement with the overview of the electrical parameters of CIGS solar cells at different temperatures given in [19]. The small decrease in FF (literature: $-0.08\%/K$ to $-0.45\%/K$) with a high standard deviation seems to be anomalous and may be attributed to the uncommon elongated shape of the PTS submodules as well as contact resistances at the connection to the SMU.

Due to the low heat capacity of the PTS with a thickness of around $100 \text{ }\mu\text{m}$, suboptimal thermo-optical properties and no active cooling available, its illuminated in-orbit operation temperature is expected to be above $120 \text{ }^\circ\text{C}$, reducing its power conversion efficiency by at least 45% when compared to room temperature conditions. In addition, the PTS is expected to be at cryogenic temperatures at the moment of leaving the eclipse and will therefore deliver significantly higher voltages for a short period of time, potentially stressing the electrical power system of the spacecraft.

The influence of vacuum on the I-V characteristic of the PTS submodules was evaluated by exposing the samples to a vacuum at a pressure of 1×10^{-5} mbar at $100 \text{ }^\circ\text{C}$ for 72 h. The before and after comparison of the exemplary I-V characteristic of sample Al 3 is provided in Figure 12.

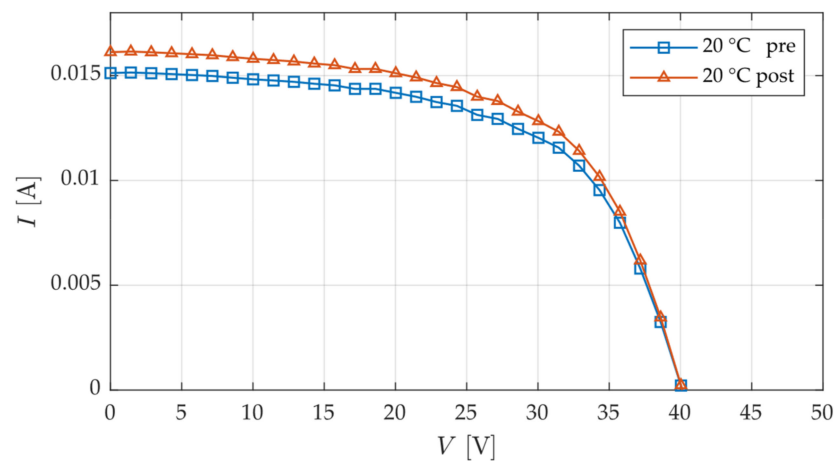


Figure 12. I-V characteristic of sample Al 3 in the fourth quadrant at 20 °C before and after the exposure to vacuum (1×10^{-5} mbar) at 100 °C for 72 h.

A significant increase in the short circuit current of the submodules of 5.1% was observed on average, while the open circuit voltage remained almost unchanged (−0.1%). As a consequence, the vacuum exposure had a positive influence on the efficiency of the submodules, which increased by an average of 5.1%. This is indicated in Table 5, which summarizes the arithmetic mean of the relative change in efficiency, fill factor, open circuit voltage and short circuit current.

Table 5. Arithmetic means of the relative change δX in different quantities X after vacuum exposure: power conversion efficiency η , fill factor FF, open circuit voltage V_{oc} and short circuit current I_{sc} ; Six PTS submodules were investigated; quantities measured at 20 °C; standard deviation σ .

Quantity X	δX [%]	σ [%]
Efficiency η	+5.139	0.958
Fill Factor FF	+0.134	0.299
Open Circuit V_{oc}	−0.133	0.273
Short Circuit I_{sc}	+5.167	0.931

The results indicate that vacuum exposure at elevated temperatures has no detrimental effect on the power output of the PTS submodules but a positive influence on their current generation, leading to a slight improvement in efficiency. However, this is not a real improvement, but a regeneration and curing effect of the CIGS solar cells, which suffer from the diffusion of atmospheric species and humidity into the different photovoltaic layers, such as the molybdenum back contact [20]. Storage of the PTS under inert atmosphere or vacuum is therefore recommended but not mandatory.

3.2. Atomic Oxygen Robustness

Using our in-house ATOX facility, two samples of each of the different material demonstrators were exposed to an atomic oxygen beam for 20 h, resulting in a total atomic oxygen fluence of $(2.05 \pm 0.31) \times 10^{19}$ Atoms/cm². This value is similar to the fluence of the planned 100 day in-orbit demonstration mission of E.T.PACK [21], which was calculated using BETsMA v2.0 [22] to be up to 1.45×10^{19} Atoms/cm². The vacuum pressure was $(1.1 \pm 0.1) \times 10^{-5}$ mbar, while the sample's temperature was (303 ± 10) K. For each sample, the I-V characteristic was measured before and after atomic oxygen exposure.

A significant change in appearance was observed only for the samples with an unprotected silver grid (Table 2, no. 1), whereas the other material combinations proved to be robust against the atomic oxygen. The degradation of a sample of the material combination 1 is shown in Figure 13.

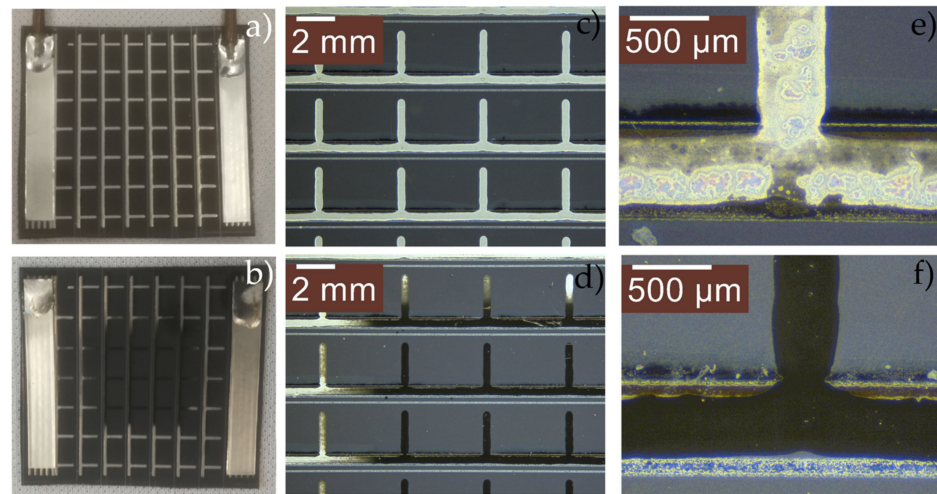


Figure 13. Degradation of a sample of material combination 1 (Table 2): (a) before the atomic oxygen test; (b) after the test, the sample was exposed to an atomic oxygen beam, restricted to a central 10 mm × 10 mm area; (c) undisturbed silver grid before the test; (d) degraded silver grid after the test; (e) partially degraded silver contact; (f) fully degraded silver contact.

The silver grid of the unprotected sample showed clear signs of oxidation. Examination of the degraded silver grid under a Hitachi TM3030 Plus electron scanning microscope (SEM) showed that the crystal grains of the silver were deformed after the test, and appeared less voluminous (see Figure 14). Despite the obvious external degradation, the samples of material combination 1 did not show any significant change in the I-V characteristic outside the range of the measurement uncertainty. This indicates that the silver was only superficially degraded during this experiment so that its electrical conductivity was not highly reduced. The I-V characteristic of the sample in Figure 13 before and after exposure to atomic oxygen is shown in Figure 15.

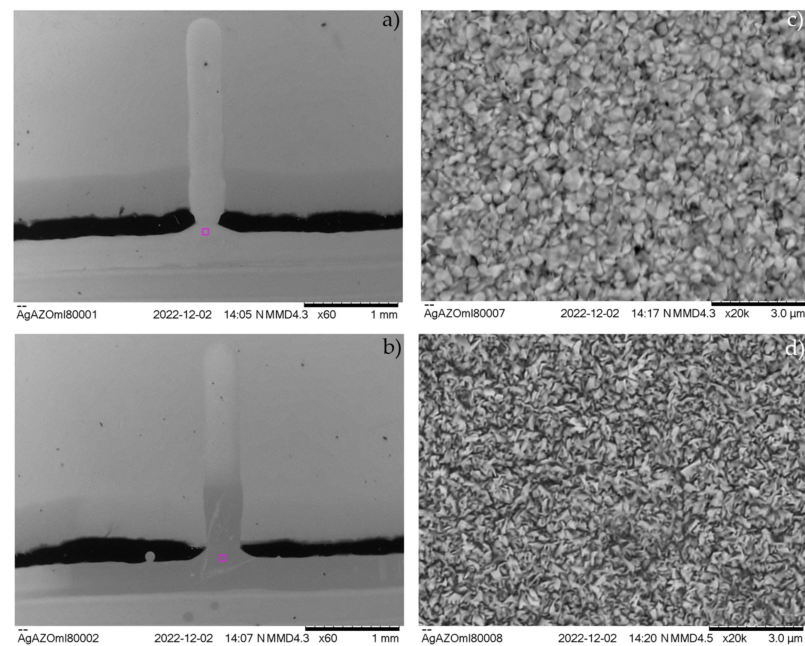


Figure 14. 15 kV secondary electron SEM image of a silver contact before and after the exposure to atomic oxygen: (a) overview of silver contact before; (b) overview of silver contact after atomic oxygen exposure; violet square shows the region of the picture sections for (c) the non-degraded silver crystal grains; and (d) the degraded silver crystal grains.

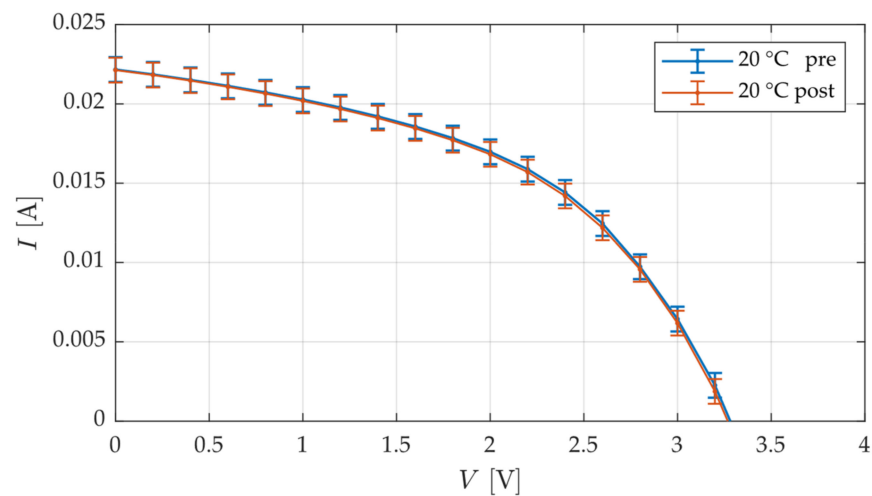


Figure 15. I-V characteristic of a material demonstrator of material combination 1 (see Figure 13) before and after atomic oxygen exposure.

The uncertainty of the current measurement was ± 0.78 mA due to the impossibility of perfectly repositioning the sample at the same location again under the SoSi with its suboptimal spatial homogeneity of irradiance.

Although the performance of the degraded sample did not decrease, the use of unprotected silver in the PTS should be avoided. Both samples with a coated silver grid (material no. 2) and a copper grid (no. 3) showed no visible degradation or loss of performance after the exposure to atomic oxygen. This was also the case for the uncoated samples with no grid at all and an ITO front contact (no. 6), which showed the lowest efficiencies. The results indicate that the use of copper ink for the electron collecting grid instead of silver is sufficient to provide robustness against atomic oxygen. However, as shown below, the coatings, which do increase the overall complexity of the system, have a beneficial effect on the thermal situation of the PTS, thus potentially increasing its in-orbit performance.

3.3. Improvement of the Thermo-Optical Properties of the PTS Using Coatings

Uncoated samples of material combination 3, as well as of combinations 4 and 5, coated with the silicate-based Sol-coating or the CAG37, respectively, were placed under the SoSi in a vacuum while their temperature curve was measured. Kapton spacers were placed between the sample and the thermal plate of the test setup to avoid thermal coupling (see Figure 16) so that the sample was thermally dominated by radiation.

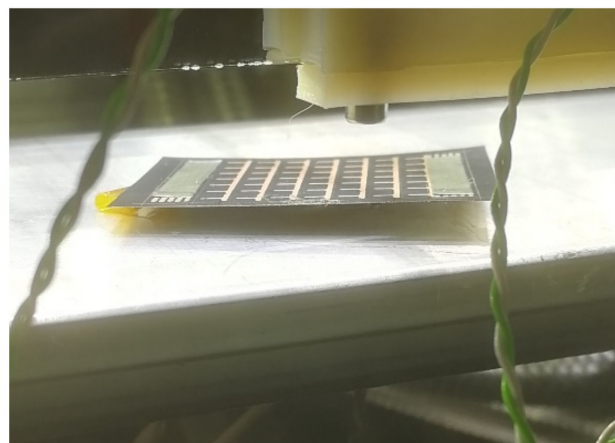


Figure 16. Non-coated sample in the test plane; Kapton spacers between thermal plate and sample to avoid thermal coupling; thermocouple type K.

The temperature was measured using a type K thermocouple attached to the back of the sample using 3M Scotchweld 2216 adhesive, and an MC USB Temp data acquisition device. The experiment was repeated three times for each sample type in order to assess the random measurement uncertainty of the system (place sample inside; generate vacuum; start SoSi and temperature measurement; switch off SoSi after 12.5 min; allow system to cool off-break vacuum; remove sample; repeat). The arithmetic means of the temperature curves of the three different samples are shown in Figure 17.

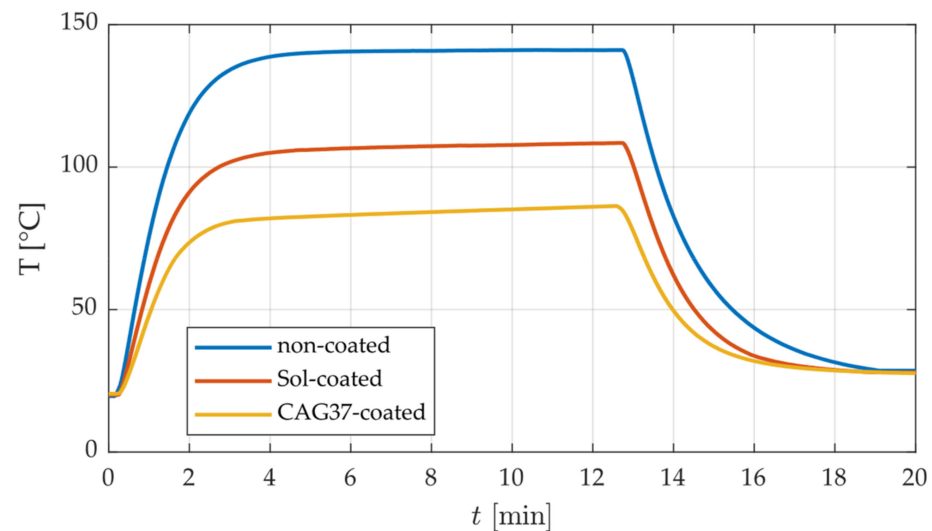


Figure 17. Heating up curves of the three tested samples; arithmetic mean values after three tests for each sample; error bars not indicated due to measurement frequency of 10 Hz.

Each sample reached a plateau after approximately 4 min. During this plateau phase, the standard uncertainty was ± 1.3 °C (uncoated), ± 1.6 °C (Sol-coated) and ± 1.2 °C (CAG37). Considering the small number of independent measurements ($n = 3$), the standard uncertainty is expanded by a factor of 4.53 for a 95 % confidence level according to the Student's *t*-distribution. This leads to a measurement uncertainty of ± 5.9 °C, ± 7.2 °C and ± 5.4 °C, respectively. The difference in temperature between the non-coated sample and the coated samples is significantly higher than the measurement uncertainty. While the uncoated samples reached a steady state temperature of 140 ± 5.9 °C after 12.5 min, the temperature of the Sol-coated samples was 106 ± 7.2 °C and the temperature of the CAG37-coated sample was 85 ± 5.4 °C.

Reducing the operating temperature by 55 K would increase the efficiency of the PTS solar cells by 25% and is therefore highly desirable. Using copper grids instead of silver should be therefore complemented by coatings that reduce the effects of the residual atmosphere and increase the thermo-optical properties of one side of the PTS.

3.4. Influence of Twisting on the PTS Performance

Using the twisting setup discussed above, the maximum power point (MPP) of the 1.5 m PTS was tracked as a function of the number of twists n over its entire length. The results are shown in Figure 18, which plots the P/P_0 ratio of the 1.5 m PTS against the number of twists n . The P/P_0 ratio describes the percentage of the MPP of the twisted PTS in comparison to the MPP of the untwisted PTS. In addition, the ratio E/E_0 is given, describing the percentage of the integral of irradiance (see Equation (3)) received by the photovoltaic side of a twisted PTS compared to a untwisted one.

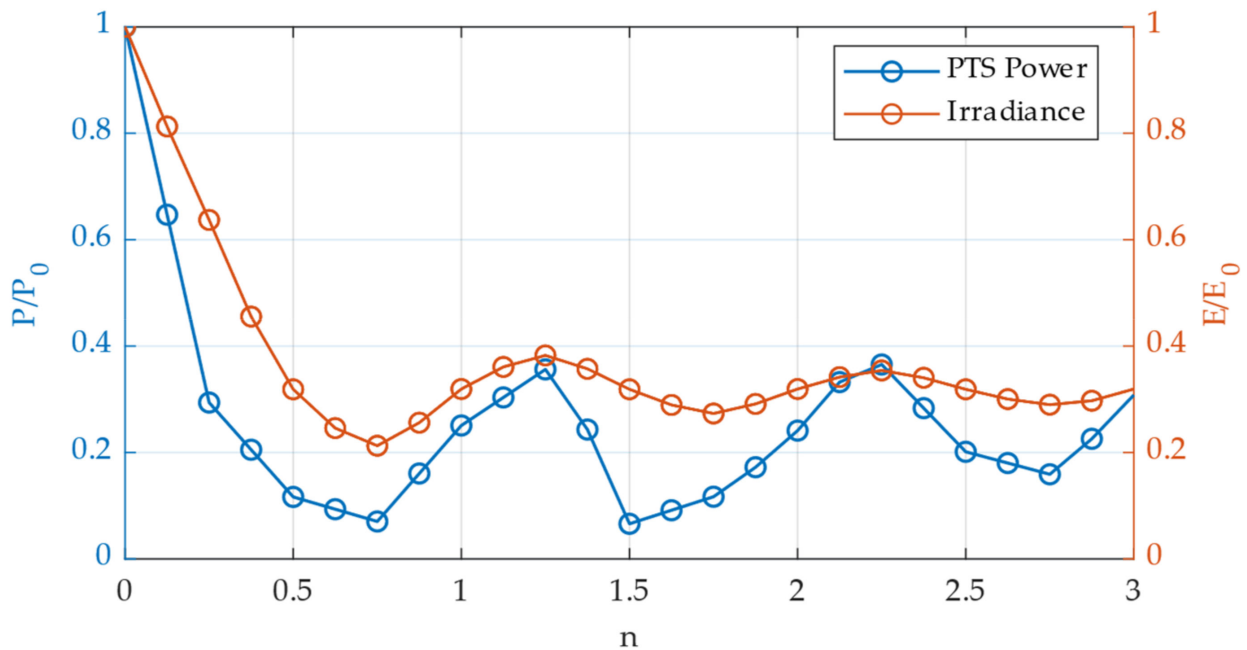


Figure 18. Comparison of the normalized maximum power P/P_0 of the 1.5 m PTS in comparison to the normalized integral of irradiance E/E_0 , received by the PTS, depending on the number of torsional twists n .

The number of twists n over the entire length L_{PTS} corresponds to one angle of rotation ($n = 1 \hat{=} 360^\circ$) at the test stand and can be converted to the number of twists per length n' :

$$n' = \frac{n}{L_{PTS}} \quad (4)$$

For example, two twists ($n = 2$) over the entire length correspond to a rotation angle of 720° and a number of twists per length of $n' = 1.33$ twists/m. Since the investigated 1.5 m PTS was a manufacturing demonstrator and originally intended for mechanical testing, its MPP under the 42 W/m^2 light source was only $2.8 \mu\text{W}$ (1.2 mW under full sun at the zenith, on 16 February 2023; 51° N) and showed a degenerated I-V characteristic. However, the twisting experiment clearly showed that the power to be expected from a twisted PTS is never higher than 32% ($1/\pi$) of the power under full illumination without twisting. Furthermore, it is not sufficient to describe these shading losses with the constant factor $1/\pi$, as it requires additional considerations. Comparing the reduction in power with the reduction in available irradiance shows that for $n = 1.25$ and $n = 2.25$, the prediction of a power reduction to 32% of the undisturbed power using Equation (3) is correct. For every other n , there is a significant difference between the experiment and theory showing a decreasing trend with increasing number of twists n . The number of twists over the entire length was limited to $n = 3$ due to the spring stiffness of the PTS, which could not be exceeded without risking permanent damage of the sample.

The results indicate that the PTS has a preferred direction of twisting, which can be attributed to an angle-dependent light reflection behavior and the architecture of the submodules. Moreover, there is a best-case and worst-case scenario of PTS twisting, depending on the number of twists per length as already discussed in [9]. Due to the serial connection of the solar cells of the submodules, their performance decreases significantly when partially shaded or illuminated with a low angle of incidence. In the absence of quantitative analysis of this phenomenon yet, a worst-case power loss of 93% ($n = 0.75$, $n = 1.5$) has to be assumed for the in-orbit power budget of an arbitrarily and uncontrollably twisted PTS. This loss could be reduced by decreasing the length of the submodules and

the number of serially connected cells, which, in turn, could adversely affect the resistive characteristics of the PTS and require the I-V matching of even more submodules.

4. Discussion

Applying thin film CIGS solar cells to one side of a 2.5 cm wide and 40 μm thick aluminum-based EDT increases its mass by 3.3 g/m. Assuming a power conversion efficiency of 5% of the PTS submodules of this study, this would result in a power gain of 1.7 W/m at 25 °C under full AM0 illumination. Since the tether itself serves as a support structure, this would translate into a specific power of $\varepsilon = 0.515$ W/g for the PTS, which is comparable to rigid InGaP/GaAs/Ge three junction solar cells ($\varepsilon = 0.4\text{--}0.8$ W/g) [23]. In addition, a correctly designed PTS can be connected directly to the electrical power system (EPS) of the spacecraft (S/C) so that no additional mass is required as long as the EPS already features MPP tracking for solar panels and the PTS power does not exceed the EPS limits.

However, the results of this study show that the submodules' efficiency of the CIGS-based PTS has an average temperature coefficient of -0.45% , resulting in a power loss of about 58% for an in-orbit operation temperature of 150 °C, which was determined for an uncoated PTS with an orbit of an inclination of 51.5° and an altitude of 600 km [24]. It should be noted that, by definition, the temperature coefficient will decrease as the efficiency of the PTS solar cells improves [19]. In addition, it has been shown that coatings of silicate- and polysilazane-based materials on one side of the PTS can effectively reduce its radiatively dominated equilibrium temperature while also protecting the solar cell stack from the residual atmosphere. The coatings, used in this study were not directly intended for the use in space; therefore, their long-term stability in a space environment has yet to be evaluated. In this context, the study by Banik et al. is therefore worth mentioning who investigated the radiative cooling properties of single layer silicon oxycarbonitride coatings for CIGS solar cells [17].

In addition to the influence of temperature on the PTS performance, there is also the influence of partial shading of its photovoltaic area. It has been shown that, in the best case, the total power of a PTS twisted uniformly along its entire length is reduced by a factor $1/\pi$. In the worst-case, the loss factor is as high as 0.07, since the arbitrary twisting of the tether in orbit and its electrical behavior cannot yet be predicted.

In the best-case scenario, this would mean that the power of the PTS would decrease by a factor of $0.58/\pi$ at 150 °C operation temperature, which corresponds to drop in effective efficiency from $\eta_0 = 5\%$ at room temperature and full illumination to $\eta_{bc} = 0.9\%$ with a corresponding specific power of 0.095 W/g. This decrease would be even more severe in the worst-case scenario with $\eta_{wc} = 0.2\%$ (0.021 W/g).

These considerations apply only to the performance of individual PTS submodules. To this date, no fully integrated PTS consisting of several submodules has been manufactured with an overall efficiency of 5% at room temperature. The I-V characteristic of the overall PTS will be highly dependent on the matching of the individual submodules. The 1.5 m PTS, intended for mechanical testing and investigated in the twisting setup of this study, consisted of poorly matched submodules and therefore showed a poor I-V characteristic with high serial and low parallel resistances, resulting in an efficiency close to zero. The manufacturing effort and the detrimental influence of the longitudinal shape of the PTS both increase directly proportional to the length of the PTS. The need for electrically matched submodules will likely require a roll-to-roll manufacturing process, which is not yet available. Power conversion losses in the spacecraft EPS will further decrease the performance of a PTS.

For a deorbit mission such as E.T.PACK Fly with a deorbit duration of 100 days [21], no significant performance degradation is expected over time due to the storage of the PTS in the S/C before operation, the high robustness of CIGS cells against particle radiation and the availability of protective coatings against atomic oxygen. However, these coatings are expected to lose transparency due to UV radiation in long-term EDT mission, e.g., for station keeping or collision avoidance. As a result, the PTS performance will degrade over time on a long time scale. This long-term degradation was not addressed in this paper and needs to be investigated in the future.

Another aspect to consider is the general orientation of the PTS in space. Since the EDT oscillates around the local vertical, the PTS can be assumed to lie within the orbital plane of the spacecraft. As a consequence, the maximum angle of light incidence available on the surface of the PTS depends on the orbital parameters of the spacecraft. This results in periodic changes of the tether illumination with the orbital frequency as well as with the frequency of the J2 perturbation.

At present, application of thin film solar cells on an EDT to harvest solar energy without the need for an additional space-consuming and heavy support structure seems feasible but insignificant in terms of energy for a propellant-less cathodic contact, due to both theoretical limits on the PTS power and practical implementation issues. The latter can be overcome by optimizing the PTS solar cell efficiency, minimizing detrimental resistances, and improving the integrity of the lateral busbars. The former, however, presents an insurmountable physical hurdle in the form of suboptimal orientation, partial shading losses due to twisting and uncontrolled high temperatures. This is especially true for the present prototype of the PTS, which is tied to the geometry of the EDT of E.T.PACK. Since the present study did not investigate PTS with different submodule geometries, future research should investigate the influence of twisting on the worst-case partial shading losses of the PTS while varying parameters such as submodule length or width. Different tether geometries should be considered in addition to a dedicated control of the PTS attitude and PTS twisting, respectively. Our results suggest that as a next step, efforts should be made to produce a fully functional PTS with an optimized I-V characteristic, consisting of multiple submodules, compatible with common satellite electrical power systems, robust to the residual atmosphere and capable of mitigating radiative heating.

Supplementary Materials: The following supporting information can be downloaded at: <https://www.mdpi.com/article/10.3390/aerospace10040386/s1>, Calibration of the Atomic Oxygen Exposure Facility. References [25–27] are cited in the supplementary materials.

Author Contributions: Conceptualization, L.P.; methodology, L.P. and M.T.; formal analysis, L.P.; investigation, L.P. and C.P.; resources, C.P.; data curation, L.P.; writing—original draft preparation, L.P.; writing—review and editing, L.P., M.T. and C.P.; visualization, L.P.; supervision, M.T.; project administration, M.T.; funding acquisition, M.T. All authors have read and agreed to the published version of the manuscript.

Funding: This research was funded by the European Space Agency, grant number ESA AO/2-1798/21/NL/GLC/ov.

Data Availability Statement: Data are contained within the article.

Acknowledgments: We gratefully acknowledge the discussions with all partners within the OSIP project, especially G. Sánchez-Arriaga, E. Lorenzini and L. Tarabini Castellani. A Consumable-less Propulsion System Based on a Bare-Photovoltaic Tether. We thank Johannes Benduhn and Kai Schmidt from the Dresden Integrated Center for Applied Physics and Photonic Materials (IAPP) for providing the Qmini RGB Photonics (Wide UV) spectrometer for the measurement of the spectrum of the Solar Simulator.

Conflicts of Interest: The authors declare no conflict of interest. The funders had no role in the design of the study; in the collection, analyses, or interpretation of data; in the writing of the manuscript; or in the decision to publish the results.

Appendix A

Table A1. Radiant power P_R at max. current, max. current I_{\max} ; operational current I_O , total number n of LEDs used.

Name	λ_p [nm]	$\Delta\lambda$ [nm]	$\theta_{1/2}$ [°]	P_R [mW]	I_{\max} [mA]	I_O [mA]	n
UVTOP270H-FW-SMD	275	11	62.5	11.5	250	250	12
DUV310-SD353EV	308	15	57.5	50	600	500	4
UVTOP340H-FW-SMD	345	10	60	40	350	350	8
UVLED-365-NC2	365	12	60	150	700	500	4
UVLED-385-NC2	385	18	75	320	700	500	4
Cree XM-LAWT-00-0000-000LT40E4	Cool White	-	60	-	3000	800	12
APG2C1-410-r2	410	20	75	400	500	500	4
SMB1N490H	490	26	65	240	350	350	4
SMB1N-690D	690	25	64	400	600	500	4
SMB1N-740D	740	22	63	290	800	500	4
SMB1N-780D	780	24	64	500	800	500	4
SMB1N-810D	810	30	63	560	800	500	4
SMB1N-830N	830	40	64	280	800	800	4
SMB1N-880	880	50	64	320	1000	800	4
SMB1N-940D	940	40	62	630	1000	500	4
SMB1N-980D	980	60	64	400	1000	800	4
SMB1N-1050GD	1050	50	64	700	1000	500	4

References

- Sánchez-Arriaga, G.; Naghdi, S.; Wätzig, K.; Schilm, J.; Lorenzini, E.C.; Tajmar, M.; Urgoiti, E.; Castellani, L.T.; Plaza, J.F.; Post, A. The E.T.PACK Project: Towards a Fully Passive and Consumable-Less Deorbit Kit Based on Low-Work-Function Tether Technology. *Acta Astronaut.* **2020**, *177*, 821–827. [CrossRef]
- Sanmartín, J.R.; Martínez-Sánchez, M.; Ahedo, E. Bare Wire Anodes for Electrodynamic Tethers. *J. Propuls. Power* **1993**, *9*, 353–360. [CrossRef]
- Lev, D.R.; Mikellides, I.G.; Pedrini, D.; Goebel, D.M.; Jorns, B.A.; McDonald, M.S. Recent Progress in Research and Development of Hollow Cathodes for Electric Propulsion. *Rev. Mod. Plasma Phys.* **2019**, *3*, 6. [CrossRef]
- Janhunen, P. Electrostatic Plasma Brake for Deorbiting a Satellite. *J. Propuls. Power* **2010**, *26*, 370–372. [CrossRef]
- Williams, J.D.; Sanmartín, J.R.; Rand, L.P. Low Work-Function Coating for an Entirely Propellantless Bare Electrodynamic Tether. *IEEE Trans. Plasma Sci.* **2012**, *40*, 1441–1445. [CrossRef]
- Sánchez-Arriaga, G.; Chen, X. Modeling and Performance of Electrodynamic Low-Work-Function Tethers with Photoemission Effects. *J. Propuls. Power* **2018**, *34*, 213–220. [CrossRef]
- Tajmar, M.; Sánchez-Arriaga, G. A Bare-Photovoltaic Tether for Consumable-Less and Autonomous Space Propulsion and Power Generation. *Acta Astronaut.* **2021**, *180*, 7. [CrossRef]
- Khan, S.B.; Sanmartín, J.R. Survival Probability of Round and Tape Tethers against Debris Impact. *J. Spacecr. Rockets* **2013**, *50*, 603–608. [CrossRef]
- Peiffer, L.; Tajmar, M.; Sánchez-Arriaga, G.; Harnisch, M.; Perfler, C. Electrical Performance Evaluation of Photovoltaic Tether Samples for Deorbit Applications. SP2022_ID282. In Proceedings of the 8th Edition of the Space Propulsion Conference, Estoril, Portugal, 9–13 May 2022.
- Bett, A.; Burger, B.; Friedrich, L.; Kost, C.; Nold, S.; Dominik, P.; Philipps, S.; Preu, R.; Rentsch, J.; Stryi-Hipp, G.; et al. Photovoltaics Report. 2022. Available online: <https://www.ise.fraunhofer.de/content/dam/ise/de/documents/publications/studies/Photovoltaics-Report.pdf> (accessed on 20 March 2023).
- Ramanujam, J.; Bishop, D.M.; Todorov, T.K.; Gunawan, O.; Rath, J.; Nekovei, R.; Artegiani, E.; Romeo, A. Flexible CIGS, CdTe and a-Si:H Based Thin Film Solar Cells: A Review. *Prog. Mater. Sci.* **2020**, *110*, 100619. [CrossRef]
- Eldada, L. Thin Film CIGS Photovoltaic Modules: Monolithic Integration and Advanced Packaging for High Performance, High Reliability and Low Cost. *Optoelectron. Integr. Circuits XIII* **2011**, *7942*, 79420F. [CrossRef]
- Mohan, M.V.A.; Pavithran, J.; Osten, K.L.; Jinumon, A.; Mrinalini, C.P. Simulation of Spectral Match and Spatial Non-Uniformity for LED Solar Simulator. In Proceedings of the 2014 IEEE Global Humanitarian Technology Conference—South Asia Satellite (GHTC-SAS 2014), Trivandrum, India, 26–27 September 2014; pp. 111–117. [CrossRef]
- Linden, K.J.; Neal, W.R.; Serreze, H.B. Adjustable Spectrum LED Solar Simulator. *Light. Diodes Mater. Devices Appl. Solid State Light. XVIII* **2014**, *9003*, 900317. [CrossRef]
- IEC 60904-9:2007; Photovoltaic Devices—Part 9: Solar Simulator Performance Requirements. International Organization for Standardization, ISO Central Secretariat: Geneva, Switzerland, 2007; pp. 1–15.

16. Schmiel, T. Entwicklung, Weltraumqualifikation Und Erste Ergebnisse Eines Sensorinstruments Zur Messung von Atomatem Sauerstoff Im Niedrigen Erdorbit. Ph.D. Thesis, TU Dresden, Dresden, Germany, 2009.
17. Banik, U.; Sasaki, K.; Reininghaus, N.; Gehrke, K.; Vehse, M.; Sznajder, M.; Sproewitz, T.; Agert, C. Enhancing Passive Radiative Cooling Properties of Flexible CIGS Solar Cells for Space Applications Using Single Layer Silicon Oxycarbonitride Films. *Sol. Energy Mater. Sol. Cells* **2020**, *209*, 110456. [[CrossRef](#)]
18. Henninger, J.H. Solar Absorptance and Thermal Emittance of Some Common Spacecraft Thermal-Control Coatings. In *NASA Reference Publication*; Goddard Space Flight Center: Greenbelt, MD, USA, 1984.
19. Theelen, M.; Liakopoulou, A.; Hans, V.; Daume, F.; Steijvers, H.; Barreau, N.; Vroon, Z.; Zeman, M. Determination of the Temperature Dependency of the Electrical Parameters of CIGS Solar Cells. *J. Renew. Sustain. Energy* **2017**, *9*, 021205. [[CrossRef](#)]
20. Theelen, M. Degradation of Cigs Solar Cells. Ph.D. Thesis, TU Delft, Delft, The Netherlands, 2015.
21. Tarabini Castellani, L.; García González, S.; Ortega, A.; Madrid, S.; Lorenzini, E.C.; Olivieri, L.; Sarego, G.; Brunello, A.; Valmorbidia, A.; Tajmar, M.; et al. Deorbit Kit Demonstration Mission. *J. Space Saf. Eng.* **2022**, *9*, 165–173. [[CrossRef](#)]
22. Sánchez-Arriaga, G.; Borderes-Motta, G.; Chiabó, L. A Code for the Analysis of Missions with Electrodynamic Tethers. *Acta Astronaut.* **2022**, *198*, 471–481. [[CrossRef](#)]
23. Verduci, R.; Romano, V.; Brunetti, G.; Yaghoobi Nia, N.; Di Carlo, A.; D'Angelo, G.; Ciminelli, C. Solar Energy in Space Applications: Review and Technology Perspectives. *Adv. Energy Mater.* **2022**, *12*, 2200125. [[CrossRef](#)]
24. Peiffer, L.; Tajmar, M. Experimental Performance Evaluation of the Photovoltaic-Bare-Tether Propulsion Concept under Space Conditions for Deorbit Applications. In Proceedings of the 73rd International Astronautical Congress (IAC), Paris, France, 18–22 September 2022.
25. Leger, L.G.; Santos-Mason, B.; Visintine, J.T.; Kuminecz, J. Review of LEO Flight Experiment. In Proceedings of the NASA Workshop on Atomic Oxygen Effects, Pasadena, CA, USA, 26–27 November 1986.
26. Willink, R. *Guide to the Expression of Uncertainty in Measurement*, 1st ed.; Cambridge University Press: Cambridge, UK, 2013; ISBN 9781139135085.
27. Banks, B.A.; Waters, D.L.; Thorson, S.D.; de Groh, K.K.; Snyder, A.; Miller, S. NASA/TM-2006-214363 Comparison of Atomic Oxygen Erosion Yields of Materials at Various Energy and Impact Angles. In Proceedings of the 10th International Symposium on Materials in a Space Environment (ISMSE), Collioure, France, 19–23 June 2006.

Disclaimer/Publisher's Note: The statements, opinions and data contained in all publications are solely those of the individual author(s) and contributor(s) and not of MDPI and/or the editor(s). MDPI and/or the editor(s) disclaim responsibility for any injury to people or property resulting from any ideas, methods, instructions or products referred to in the content.